Finite-temperature force constants are essential for accurately predicting the thermal conductivity of rutile TiO_2

Bo Fu [1,2] Guihua Tang [1,*] and Alan J. H. McGaughey [2,†]

[1]*MOE Key Laboratory of Thermo-Fluid Science and Engineering, School of Energy and Power Engineering, Xi'an Jiaotong University, Xi'an 710049, China*

[2]*Department of Mechanical Engineering, Carnegie Mellon University, Pittsburgh, Pennsylvania 15213, USA*

(Received 17 June 2021; accepted 13 December 2021; published 13 January 2022)

Phonon transport in rutile TiO_2 between temperatures of 100 and 900 K is investigated using lattice dynamics calculations and the Boltzmann transport equation. Zero- and finite-temperature force constants are extracted from density functional theory calculations to examine the effects of finite temperature on phonon properties and thermal conductivity. Using the zero-temperature force constants leads to thermal conductivity predictions along the *a* and *c* axes that are 50% lower than experimental measurements at a temperature of 300 K. The underprediction increases as the temperature is further increased. Using temperature-specific force constants, however, leads to thermal conductivity predictions that fall within the uncertainty bounds of multiple sets of experimental measurements. Phonon mode analysis reveals that the thermal conductivity underprediction from the zero-temperature force constants is a result of an underprediction of phonon lifetimes. The lifetime underprediction results from the temperature dependence of (i) the second-order force constants, which set the phonon frequencies and thus the three-phonon scattering phase space, and (ii) the third-order force constants, which influence the intrinsic scattering rates. Our results emphasize the importance of including finite-temperature effects when studying phonon transport in oxides and inform how nanostructuring impacts the thermal conductivity of rutile TiO_2.

DOI: 10.1103/PhysRevMaterials.6.015401

I. INTRODUCTION

Titanium dioxide (TiO_2) is a promising material in applications including photocatalysis [1–3], solar cells [4], lithium ion batteries [5,6], pigments [7], amphiphilic surfaces [8], microwave radiation-assisted synthesis [9], and thermoelectrics [10]. TiO_2 naturally occurs in rutile, anatase, and brookite phases. Rutile is the most common and stable phase at temperatures below 1800 K [11]. While the optical and electronic properties of rutile TiO_2 have been extensively studied [12–16], measurements and predictions of its thermal properties are limited [17–24]. Understanding the carrier-level behavior that leads to measured thermal conductivities is essential in the design of energy conversion devices using heat (e.g., thermoelectrics) and in developing thermal management strategies in any application where there is excess heat generation, particularly when the TiO_2 is nanostructured.

Rutile TiO_2 has a tetragonal unit cell and the $P4_2/mnm$ space group, as shown in Fig. 1(a). The structure is anisotropic, with the *c*-axis lattice constant larger than the *a*-axis lattice constant. Around room temperature, the thermal conductivity of rutile TiO_2 has been measured by comparative [17,18], two-heater [19], and time-domain thermoreflectance (TDTR) [20] methods. The measured values are collected in Table I. The *c*-axis thermal conductivity is always higher than that of the *a* axis. Charvat and Kingery [18], Yoshida [21], Koenig [22], Ok *et al.* [23], and Touloukian [24] reported measured thermal conductivities at higher temperatures and Thurber and Mante [19] reported data at lower temperatures, all of which are plotted in Figs. 2(a) and 2(b). Given the wide spread of the measured values at any given temperature and the measurement uncertainties, theoretical predictions are needed to provide fundamental benchmarks and to elucidate the underlying thermal transport physics.

In rutile TiO_2, which can be an electrical insulator or a semiconductor, the dominant heat carriers are phonons. Recently, a phonon-based computational framework [25–32] has been widely employed to predict thermal conductivity. In the framework, harmonic and anharmonic force constants (FCs) are extracted from first-principles density functional theory (DFT) and/or density functional perturbation theory (DFPT) calculations. Using the harmonic FCs, harmonic lattice dynamics calculations are performed to obtain the phonon frequencies and eigenvectors. The harmonic properties and the anharmonic FCs are then used to determine phonon scattering rates with perturbation theory (e.g., due to interactions with other phonons or defects) and/or empirical models (e.g., the Fuchs-Sondheimer model for phonon-boundary scattering). With the full set of phonon properties, the Boltzmann transport equation (BTE) is then solved for the phonon distribution function and thermal conductivity. This parameter-free framework has enabled agreement between predictions and measurements for diverse crystalline materials over a wide range of temperatures, e.g., silicon [25,33], diamond [34],

*ghtang@mail.xjtu.edu.cn
†mcgaughey@cmu.edu

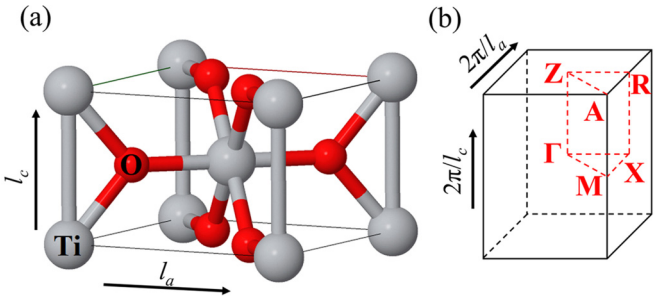

FIG. 1. Rutile TiO_2 (a) atomic structure and (b) corresponding first Brillouin zone and its high-symmetry points including **Z** (0,0,0.5) (reduced coordinates), **A** (0.5,0.5,0.5), **M** (0.5,0.5,0), **R** (0,0.5,0.5), and **X** (0,0.5,0).

and compound semiconductors [35]. The framework has also been employed to study two-dimensional materials such as graphene [36] and phosphorene [37].

For oxides, however, this computational framework has seen limited application [38–44] and less success. The challenges may originate from the following: (i) Atomic structures with large unit cells and/or low symmetry (e.g., brookite TiO_2 [45], β-Ga_2O_3 [40]), which lead to large computational cost. (ii) Naturally occurring oxygen vacancies may result in an overprediction of measured thermal conductivities (e.g., in $SrTiO_3$ [41]). (iii) The temperature dependence of the phonon frequencies. Recent studies have demonstrated the importance of including temperature-dependent phonon frequencies in making accurate predictions of the optical properties of MgO [46] and α-Al_2O_3 [42]. Our objective here is to examine the effect of (iii) on thermal conductivity predictions for rutile TiO_2, whose phonon frequencies have a significant temperature dependence [47,48].

The harmonic phonon properties of rutile TiO_2 have been studied using input from first-principles calculations [47,48,51–54]. Harmonic FCs are typically extracted using finite differences on structures with displaced atoms or from DFPT. Such calculations are based on the zero-temperature energy surface and lead to what we will refer to as the 0 K FCs. Montanari and Harrison [53] examined the effect of the exchange-correlation functional in DFT calculations on the phonon frequencies of rutile TiO_2 using the finite-difference method. They found that the generalized-gradient approximation from Perdew-Burke-Ernzerhof overestimated the zero-pressure lattice constants and predicted imaginary transverse optical modes, which indicates an unstable structure. No imaginary modes were found using the local density approximation (LDA). Through DFPT calculations with the LDA, Mitev *et al.* [54] showed that isotropic tension or anisotropic compression/tension led to significant softening of the transverse acoustic (TA) modes and eventually imaginary frequencies. Wehinger *et al.* [47] experimentally observed a significant temperature dependence of the TA mode frequencies. Their DFPT calculations revealed an underestimation of the TA frequency along the Γ-**Z** and **M**-**A** directions in the first Brillouin zone [Fig. 1(b)]. The strain- and temperature dependencies of the phonon frequencies of rutile TiO_2 indicate the importance of anharmonicity, which leads to thermal expansion and atomic oscillations in an anharmonic energy well.

The impact of thermal expansion can be partially included by using finite-temperature lattice constants in the harmonic framework (i.e., the quasiharmonic approximation). This approach, however, will predict imaginary frequencies for structures that are not stable at zero temperature. For rutile TiO_2, Lan *et al.* [48] demonstrated the failure of the quasiharmonic approximation by predicting imaginary phonon frequencies at a temperature of 1373 K. They then used the temperature-dependent effective potential (TDEP) method [55–57] to extract finite-temperature FCs from *ab initio* molecular dynamics simulations. By doing so, they were able to computationally reproduce the temperature-dependent acoustic phonon frequencies and phonon density of states measured from inelastic neutron scattering. The only first-principles-based thermal conductivity prediction for rutile TiO_2 used 0 K FCs [58].

In the TDEP method, which was developed by Hellman and co-workers [55–57], finite-temperature FCs are extracted from atomic force–displacement data sets obtained from molecular dynamics simulations or stochastic sampling [59,60]. Using finite-temperature FCs allows for a direct sampling of the effective potential surface at each finite temperature considered. By using the TDEP method, the importance of finite-temperature FCs has been shown through accurate predictions of thermal conductivity in materials such as Bi_2Te_3 [61], lead chalcogenides [59], and AlN [62].

In this work, we perform first-principles and lattice dynamics calculations combined with an iterative or direct solution of the BTE to study the thermal conductivity and phonon properties of rutile TiO_2 at temperatures ranging from 100 to 900 K. Finite-temperature harmonic and cubic FCs are extracted by the TDEP method, such that we remove all approximations associated with temperature. We also extracted the 0 K FCs to assess their validity. We first compare the predicted thermal conductivities of rutile TiO_2 using different sets of force constants with available experimental data. The use of finite-temperature FCs leads to accurate predictions, while significant underpredictions are found when using the 0 K FCs. The mode-dependent phonon frequencies, group velocities, and lifetimes are then analyzed to reveal the fundamental reasons for why finite-temperature FCs are essential.

II. METHOD

From the linearized BTE and the Fourier law, the thermal conductivity k_α in direction α can be expressed as [25]

$$k_\alpha = \sum_{\kappa,\nu} c_{\mathrm{ph}} v_{\mathrm{g},\alpha}^2 \tau_\alpha. \quad (1)$$

For each phonon mode identified by wave vector κ and polarization branch ν, the volumetric specific heat, c_{ph}, and the α component of the group velocity vector, $v_{\mathrm{g},\alpha}$, are obtained from harmonic lattice dynamics calculations. τ_α is the phonon lifetime as heat flows along the α direction. Three-phonon scattering is included by using anharmonic lattice dynamics calculations combined with the BTE. Phonon-isotope scattering leads to a reduction in thermal conductivity of 3% at

a temperature of 100 K (where it will be most pronounced) and is thus not included in the reported data. No other phonon scattering mechanisms are included.

System energies and atomic forces are obtained from DFT calculations using the VASP package [63,64]. The LDA exchange-correlation functional [65] and projector augmented wave pseudopotentials [64] are employed in all calculations. Similar to previous works [53,66], we found that the Perdew-Burke-Ernzerhof exchange-correlation functional overestimates the lattice constants and leads to imaginary phonon frequencies at zero temperature.

The equilibrium zero-temperature atomic structure of rutile TiO_2 is obtained through an energy minimization using DFT calculations with a plane-wave cutoff of 500 eV and an electronic wave vector grid of $6 \times 6 \times 6$. The lattice constants and the internal coordinates are allowed to vary. The a-axis and c-axis lattice constants are $l_a = 4.554$ Å and $l_c = 2.922$ Å, respectively. The value of u is 0.3039, which can be used to specify the internal coordinates. The coordinates of the four oxygen atoms are $(ul_a, ul_a, 0)$, $[(1\text{-}u)l_a, (1\text{-}u)l_a, 0]$, $[(0.5\text{-}u)l_a, (0.5+u)l_a, 0.5l_c]$, and $[(0.5+u)l_a, (0.5\text{-}u)l_a, 0.5l_c]$, while those of the two titanium atoms are (0,0,0) and $(0.5l_a, 0.5l_a, 0.5l_c)$, as shown in Fig. 1(a). The finite-temperature atomic structures are taken from the LDA *ab initio* molecular dynamics simulations of Lan *et al.* [48].

The 0 K harmonic and cubic FCs are extracted from the finite displacement method [67]. The atomic forces are calculated by building a $3 \times 3 \times 5$ supercell and moving one or two atoms with a displacement of 0.03 Å. The convergence of the 300 K thermal conductivity based on the zero-temperature FCs with the supercell size is shown in Table S1 of the Supplemental Material [68]. The electronic wave vector grid is $2 \times 2 \times 2$ and the plane-wave cutoff is 500 eV. Born effective charges and dielectric constants are obtained from DFPT calculations to include long-range interactions. A direct solution of the linearized BTE is used to calculate the phonon properties and thermal conductivity with a phonon wave vector grid of $15 \times 15 \times 25$. Further increasing the resolution changes the predicted thermal conductivities by less than 1%. The extraction of the zero-temperature FCs, the lattice dynamics calculations, and the direct BTE solutions are performed using the PHONO3PY package [67].

The finite-temperature FC extraction and the subsequent lattice dynamics calculations and BTE solutions are performed with the TDEP package [55–57]. The stochastic sampling approach developed by Shulumba *et al.* [59,60] is used to include Bose-Einstein statistics and to reduce the required DFT calculations compared to running *ab initio* molecular dynamics simulations. In the stochastic scheme, an iterative procedure is used to converge the FCs. The FCs are initialized using the Debye temperature and then used to generate a series of $3 \times 3 \times 5$ supercells. The convergence of the 300 K thermal conductivity based on the 300 K FCs with the supercell size is shown in Table S1. The force-structure data set is built by calculating the atomic forces in DFT calculations. The FCs are then updated using a least-squares-fitting method. In our calculations of rutile TiO_2, 128 supercells are generated in each step and the FCs are converged such that the maximum change of the phonon frequencies is less than 3% after seven iterations. The harmonic (cubic) cutoff is 6.0 (4.0) Å. The DFT calculation parameters are the same as those when extracting the 0 K FCs. Lattice dynamics calculations with an iterative solution of the BTE are performed to calculate phonon properties and thermal conductivity with a phonon wave vector grid of $15 \times 15 \times 25$. Further increasing the resolution changes the predicted thermal conductivities by less than 2%. Results from the convergence tests for both TDEP and the 0 K FCs are plotted in Fig. S1. The predicted thermal conductivities based on the relaxation-time approximation are $<3\%$ smaller than the iterative/direct results for both the 0 K and the 300 K FCs, showing the dominance of umklapp scattering. All the reported data are based on the iterative/direct BTE solutions.

III. RESULTS AND DISCUSSION

A. Thermal conductivity

The thermal conductivities of rutile TiO_2 predicted at a temperature of 300 K from the 0 and 300 K FCs are provided in Table I. Both calculations show the expected anisotropy, with a higher thermal conductivity along the c axis. The a-axis (c-axis) thermal conductivity from the 0 K FCs, however, is 52% (51%) smaller than that from the 300 K FCs. The a-axis (c-axis) thermal conductivity from the 300 K FCs is 7% larger (4% smaller) than the two-heater result [19] and 15% (8%) larger than the TDTR result [20]. Our predictions fall within the reported uncertainties for both measurements. The 0 K FCs underpredict the a-axis (c-axis) thermal conductivity by 49% (53%) compared to the two-heater results [19] and by 45% (47%) compared to the TDTR results [20].

The predicted thermal conductivities at temperatures between 100 and 900 K are plotted in Figs. 2(a) and 2(b) along with previous measurements that span the full temperature range. Three sets of predictions are plotted, each with thermal conductivity evaluated in increments of 50 K. In the first, denoted as "Temperature-Specific FCs" by the solid blue curve, the thermal conductivity is predicted by using the TDEP force constants at each temperature. We first discuss the results for the a axis. At temperatures below 200 K, the predictions are more than 20% higher than the measured values from Thurber and Mante [19]. A similar divergence at low temperatures was observed in $SrTiO_3$ [41]. At low temperatures, phonon transport is sensitive to impurity scattering. Oxides like $SrTiO_3$ and TiO_2 have a natural oxygen deficiency [19,69], which we suggest to be the origin of our low-temperature overprediction. Between temperatures of 200 and 300 K, the predictions are less than 20% higher than the results from Thurber and Mante [19]. Above room temperature, the predictions agree well with the measurements from Thurber and Mante [19], Koenig [22], Ok *et al.* [23], Yoshida [21], McCarthy and Ballard [17], and Jiang *et al.* [20]. Between temperatures of 400 and 900 K, the predictions are 13%–41% smaller than the measured values from Charvet and Kingery [18]. The predicted thermal conductivity shows a $T^{-0.697}$ temperature dependence, close to the $T^{-0.691}$ measured by Charvat and Kingery [18] but stronger than the $T^{-0.474}$ scaling reported by Ok *et al.* [23]. Our results suggest that it is sufficient to consider three-phonon scattering in predicting the thermal conductivity of rutile TiO_2.

TABLE I. Thermal conductivity of rutile TiO_2 around room temperature from previous measurements [17–20] and the present predictions with 0 and 300 K force constants (FCs).

Method		Temperature (K)	Direction	Thermal conductivity (W/m K)
Measurement	Comparative [17]	317	*a* axis	8.8
		309	*c* axis	12.5
	Two-heater [19]	300	*a* axis	7.0 ± 0.5
		300	*c* axis	10.4 ± 0.7
	TDTR [20]	300	*a* axis	6.5 ± 2.0
		300	*c* axis	9.3 ± 1.1
Prediction	0 K FCs	300	*a* axis	3.6
		300	*c* axis	4.8
	300 K FCs	300	*a* axis	7.5
		300	*c* axis	10.0

In the second data set, denoted as 0 K FCs by the dash-dotted blue curve, the 0 K FCs are used to predict thermal conductivity over the full temperature range. The result is a large underprediction compared to the thermal conductivities from both the temperature-specific FC predictions and the measurements. The underprediction compared to the temperature-specific FCs increases with increasing temperature and is 52% at 300 K, 61% at 600 K, and 65% at 900 K. This finding demonstrates the strong finite-temperature effects on the force constants and thus thermal conductivity of rutile TiO_2 [70]. Mitra *et al.* [50] also predicted lower thermal conductivities at temperatures between 250 and 400 K by employing 0 K FCs, which are plotted as a dash-dotted green line in Fig. 2(a).

In the third data set, denoted as 300 K FCs and plotted as a dashed blue curve, the 300 K FCs are used to predict the thermal conductivity between temperatures of 300 and 900 K. As the temperature increases to 600 K, the 300 K FCs predict a thermal conductivity that is 22% smaller than the value from the 600 K FCs. At 900 K, the underprediction from 300 K FCs increases to 29%. Consistent with the 0 K FC predictions, these results indicate that using force constants extracted at lower temperatures will underpredict the thermal conductivity at higher temperatures.

Predicted and measured thermal conductivities along the *c* axis at temperatures between 100 and 900 K are plotted in Fig. 2(b). For the temperature-specific FCs, the predictions below a temperature of 130 K are more than 20% larger than the measurements from Thurber and Mante [19], similar to the *a*-axis results in Fig. 2(a). At temperatures between 200 and 300 K, the predictions agree well with the measurements from Thurber and Mante [19] and Jiang *et al.* [20]. Above a temperature of 300 K, the predictions are <23% larger than the measurements from Touloukian [24] but 18%–31% smaller than those from Charvat and Kingery [18]. From 400 to 900 K, the predicted temperature dependence, $T^{-0.694}$, is close to the $T^{-0.597}$ scaling measured by Charvat and Kingery [18] and $T^{-0.829}$ from Touloukian [24]. Similar to the *a*-axis results, the 0 K FCs underpredict the thermal conductivity compared to the measurements and the predictions of temperature-specific FCs and the 300 K FCs underpredict thermal conductivity at temperatures above 300 K.

We conclude that (i) 0 K FCs significantly underpredict the thermal conductivity of rutile TiO_2 between temperatures

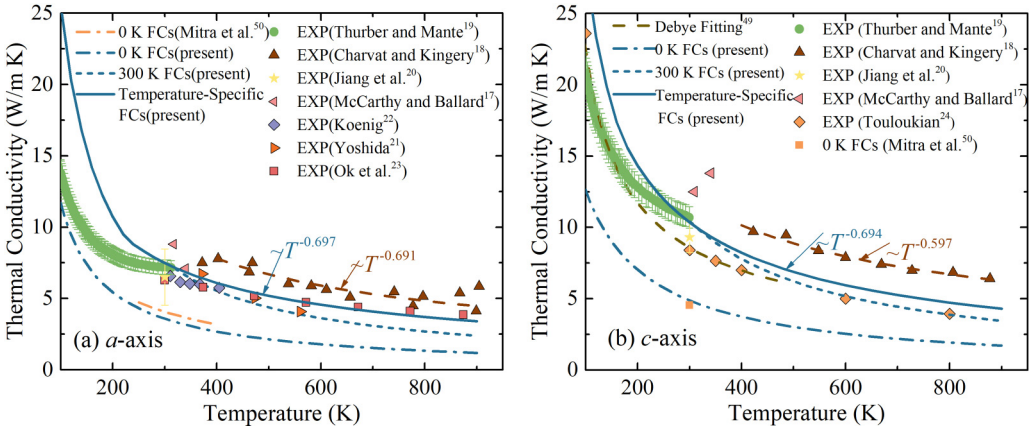

FIG. 2. (a) *a*-axis and (b) *c*-axis thermal conductivities of rutile TiO_2 versus temperature from 100 to 900 K. The measurements are from McCarthy and Ballard [17], Charvat and Kingery [18], Thurber and Mante [19], Jiang *et al.* [20], Yoshida [21], Koenig [22], Ok *et al.* [23], and Touloukian [24]. A Debye fitting [49] for Touloukian's data and a prediction based on the 0 K FCs from Mitra *et al.* [50] are also provided. Three sets of predictions from the calculations presented here use the temperature-specific, 300 K, and 0 K FCs.

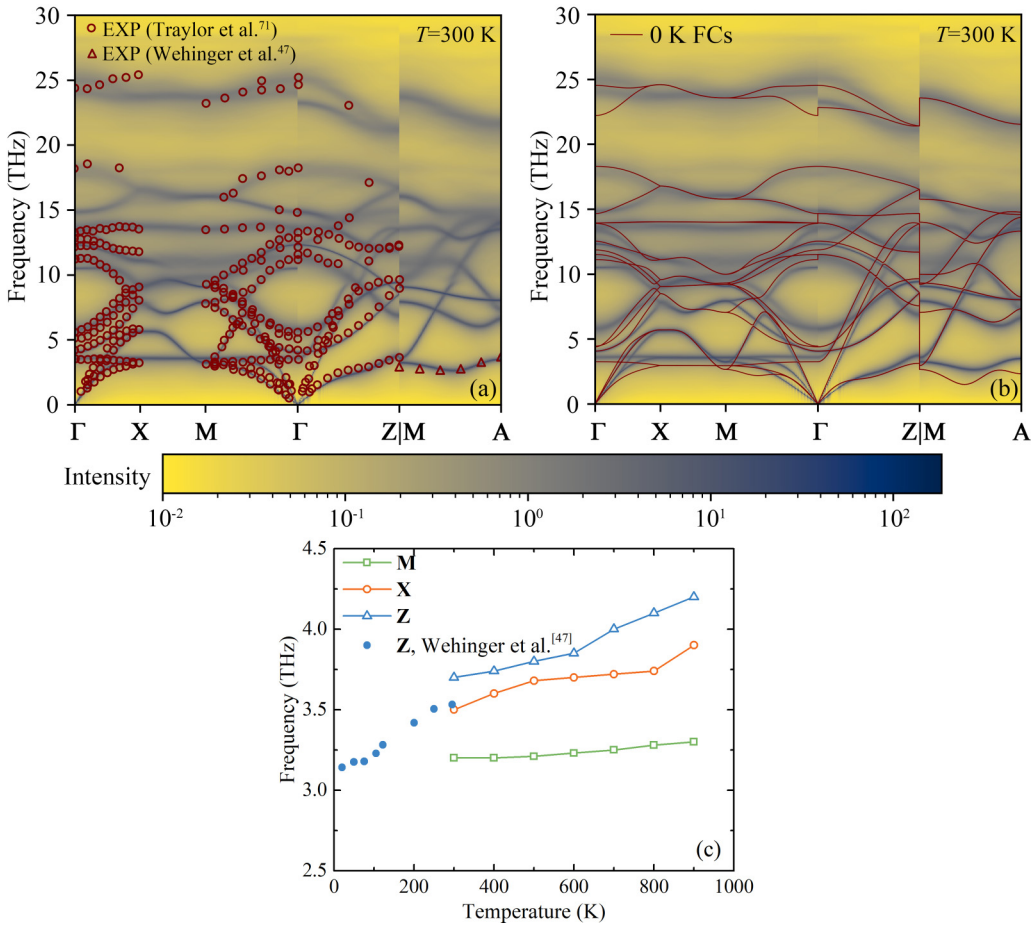

FIG. 3. Phonon spectral function at a temperature of 300 K plotted with (a) measured values from inelastic neutron scattering (open circles) [71] and inelastic x-ray scattering (open triangles) [47] and (b) phonon dispersion obtained from the 0 K FCs. (c) Predicted frequency of the TA phonon mode at the **M**, **X**, and **Z** points [Fig. 1(b)] plotted as a function of temperature. The measurements from Wehinger *et al.* [47] are also plotted.

of 100 and 900 K. (ii) By extracting force constants at each finite temperature, the predictions capture the magnitudes of the measurements. Above room temperature, good agreement between predictions and measurements is achieved. (iii) Using force constants extracted at finite but lower temperatures leads to an underprediction of thermal conductivity at higher temperatures. In the next section, we explore the mode-level phonon properties to reveal the origin of these findings.

B. Phonon spectral function

To start, we will examine the phonon frequencies using the phonon spectral function [48,59,60], which starts from the harmonic phonon dispersion and includes the frequency shifts and broadening that result from anharmonicity. The intensity of a point represents the probability that a phonon mode exists at that frequency (vertical axis) and wave vector (horizontal axis). The phonon spectral function along high-symmetry directions calculated by TDEP at a temperature of 300 K is plotted in both Figs. 3(a) and 3(b). The spectral functions at temperatures of 600 and 900 K are plotted in Figs. S3(a) and S3(b).

Measured phonon frequencies are also plotted in Fig. 3(a). Along the Γ-**X**, Γ-**M**, and Γ-**Z** directions, the spectral function peaks agree with the phonon frequencies measured by inelastic neutron scattering (open circles) by Traylor *et al.* [71] at a temperature of 300 K. Along the **M**-**A** direction, Wehinger *et al.* [47] observed a minimum for the TA branch using inelastic x-ray scattering at a temperature of 295 K. Their measurements are plotted as open triangles in Fig. 3(a). Our predictions reproduce the measured frequencies and the minimum.

In Fig. 3(b), the harmonic phonon dispersion predicted from the 0 K FCs is plotted along with the 300 K spectral function. There are large differences for low-frequency phonons along the Γ-**X**-**M**-Γ loop and the **M**-**A** direction, with the 0 K FCs predicting smaller frequencies for the TA and the lowest optical branches. Along the Γ-**M** direction, the measurements [Fig. 3(a)] and the spectral function show a degeneracy of the TA branch at a temperature of 300 K that is not predicted by the 0 K dispersion near the Γ point. Along the **M**-**A** direction, the TA branch for the 0 K dispersion has a maximum near the **A** point that is not present in the spectral function or the measurements. The **M**-**A** TA frequencies for the 0 K dispersion are also smaller than the spectral function. For other branches, the 0 K dispersion and 300 K spectral functions have similar magnitudes and shapes, except for the highest optical branches along the Γ-**X** direction.

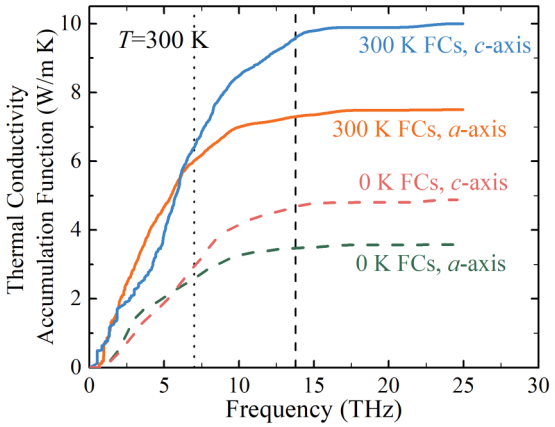

FIG. 4. Frequency-dependent thermal conductivity accumulation functions predicted from 0 and 300 K FCs at a temperature of 300 K. The vertical dotted line at 7 THz indicates the highest acoustic phonon frequency along the Γ-**X** and Γ-**M** directions. The vertical dashed line at 14 THz indicates the highest acoustic phonon frequency along the Γ-**Z** direction.

To examine the temperature dependence of the spectral function, the TA frequencies at the **X**, **M**, and **Z** points are extracted by finding the spectral function peaks. The results are plotted in Fig. 3(c) from 300 to 900 K. The **Z** and **X** point frequencies increase by 0.4 and 0.5 THz over this range, respectively, while the **M** point frequency increases by 0.1 THz. A similar temperature dependence is obtained for the lowermost optical branches. The predicted frequency increase for these low-frequency phonons is similar to the measured results at lower temperatures from Wehinger *et al.* [47]. Furthermore, as temperature increases, the modes broaden due to the increased anharmonicity, especially for the optical branches. We hypothesize that the temperature dependence of the phonon frequencies is one of the origins of the thermal conductivity underprediction observed when using the 0 K FCs.

C. Thermal conductivity accumulation function

To test this hypothesis, the thermal conductivity contribution from each phonon mode can be examined using the modal heat capacities, group velocities, and lifetimes. The thermal conductivity accumulation functions as a function of frequency calculated by the 0 and 300 K FCs at a temperature of 300 K are plotted in Fig. 4. The vertical coordinate of any point on the accumulation function represents the thermal conductivity contribution from phonon modes with frequencies less than the horizontal coordinate of that point (i.e., it is a cumulative distribution function). The vertical dotted line at 7 THz indicates the highest acoustic phonon frequency along the Γ-**X** and Γ-**M** directions. The vertical dashed line at 14 THz indicates the highest acoustic phonon frequency along the Γ-**Z** direction. Some optical modes also have frequencies below 14 THz. More than 95% of the total thermal conductivity is contributed by phonon modes with frequencies below 14 THz for the 0 and 300 K FCs along both the *a* and *c* axes. The accumulations for the 300 K FCs rise faster than those for the 0 K FCs across this frequency range, which is the origin of the underprediction. To understand how nanostructuring will impact thermal transport, the thermal conductivity accumulation functions as a function of mean free path are plotted in Fig. S5.

D. Phonon group velocities and lifetimes

To identify the origin of the reduced contribution from low-frequency phonons when using the 0 K FCs, we examine the phonon properties. For the specific heat, increasing a mode's frequency (as happens with some modes when using the 300 K FCs) decreases its population, leading to a smaller specific heat and a smaller contribution to thermal conductivity. The group velocities calculated using the 0 and 300 K FCs are plotted in Fig. 5(a). The two data sets have similar distributions, with the major differences at low frequencies. Around a frequency of 3.0 THz, there is a cluster of group velocities corresponding to the 0 K FCs (blue markers). Around a frequency of 3.6 THz, there is a similar clustering of the group velocities corresponding to the 300 K FCs (red markers). This frequency shift corresponds to the discrepancy between the 0 and 300 K dispersions plotted in Fig. 3(b). The 0 K FCs predict group velocities that are, on average, 6% larger than those from the 300 K FCs for modes with the group velocities greater than 7000 m/s. A larger group velocity corresponds to a larger contribution to thermal conductivity, which is proportional to the square of the group velocity. The specific heat and group velocity are therefore not the reason why the 0 K FCs underpredict thermal conductivity. The group velocities obtained from the 600 and 900 K FCs are plotted in Fig. S4. The group velocities from 300 K FCs are, on average, 1% and 3% larger than those from 600 K FCs and 900 K FCs.

The *a*-axis direction phonon lifetimes at a temperature of 300 K calculated using the 0 and 300 K FCs are plotted in Fig. 5(b). The 300 K FCs predict larger lifetimes than the 0 K FCs for low-frequency phonons. By scaling the lifetimes as ω^{-2}, the prefactor for the 0 K FCs is 75% smaller than that for the 300 K FCs. For a specific phonon mode, a larger lifetime corresponds to a larger contribution to thermal conductivity. Recall from Fig. 5(a) that the 0 K FCs predict higher group velocities for low-frequency phonons than the 300 K FCs. Therefore, the underprediction of the lifetimes by the 0 K FCs must be the cause of the accompanying underprediction of thermal conductivity. We find similar results when analyzing the *c*-axis direction lifetimes. Gu *et al.* [72] reported that using 0 K FCs significantly underpredicted the four-phonon lifetimes in graphene, which is similar to our finding for rutile TiO_2.

The *a*-axis direction lifetimes calculated by the 300 and 600 K FCs at a temperature of 600 K are plotted in Fig. S6(a). The 600 K FCs predict higher lifetimes than the 300 K FCs for low-frequency phonons. This result is consistent with the 300 K FCs underpredicting thermal conductivity at temperatures above 300 K, as shown in Figs. 2(a) and 2(b). We conclude that for rutile TiO_2, using low-temperature FCs leads to an underprediction of phonon lifetimes at higher temperatures, which results in an underprediction of thermal conductivity.

Phonon lifetimes are determined by the phonon scattering phase space and strength. The phonon scattering phase

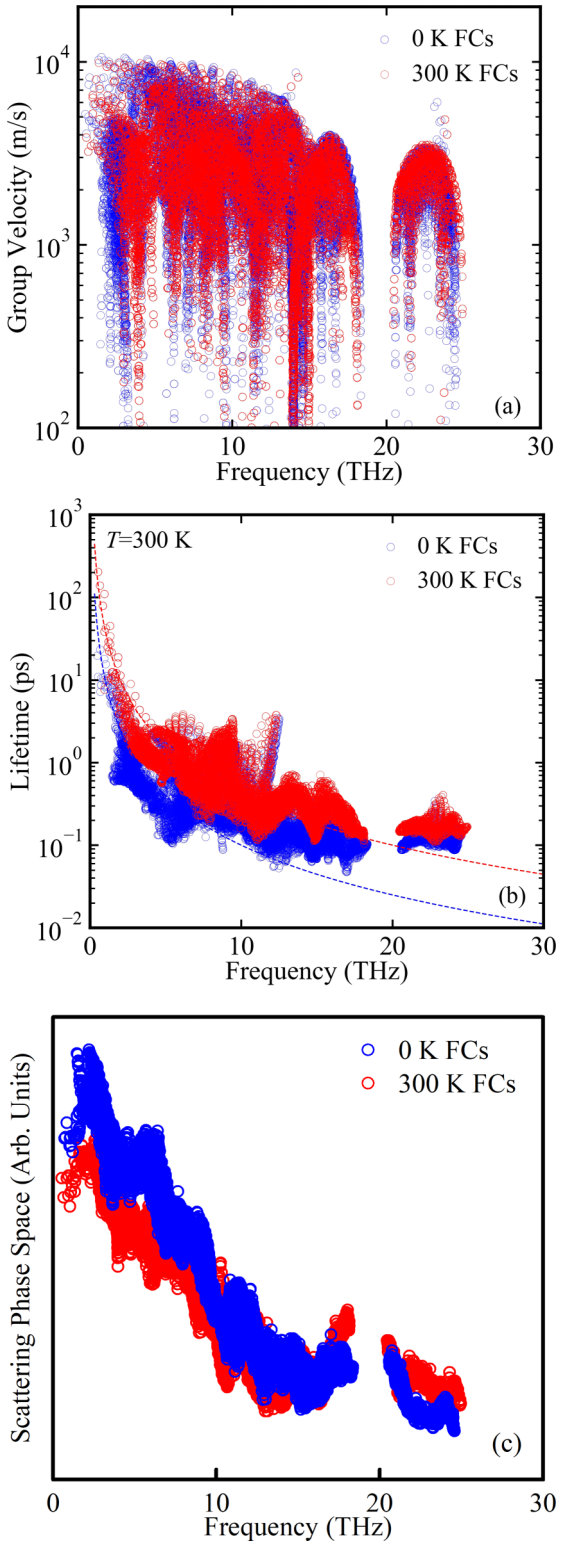

FIG. 5. (a) Phonon group velocities, (b) 300 K lifetimes, and (c) three-phonon scattering phase space obtained from the 0 K FCs and 300 K FCs plotted versus frequency. The dashed lines in (b) show a ω^{-2} scaling.

space is calculated by counting the number of phonon-phonon scattering processes that satisfy the phonon energy and momentum conservation selection rules [73]. It is thus a property that can be calculated using the harmonic FCs. A larger number of possible phonon-phonon scattering events will lead to lower lifetimes. The scattering strength is related to the harmonic and anharmonic properties.

The three-phonon scattering phase space calculated by the 0 and 300 K FCs is plotted in Fig. 5(c). For frequencies smaller than 10 THz, the 300 K FCs predict a smaller phase space than the 0 K FCs, which is consistent with the higher phonon lifetimes [Fig. 5(b)]. For frequencies ranging from 10 to 19 THz, the 300 K FCs and 0 K FCs predict a similar phase space. For frequencies higher than 20 THz, the phase space from the 0 K FCs is smaller. Therefore, the larger phase space from 0 K FCs contributes to the underprediction of the lifetimes for low-frequency phonons.

The three-phonon scattering phase space calculated by the 300 and 600 K FCs is plotted in Fig. S6(b). The two data sets closely overlap. The 300 K FCs underpredict the lifetimes of the low-frequency phonons at 600 K, however, which indicates that the scattering strength also contributes to the underprediction.

IV. CONCLUSIONS

We investigated the thermal conductivity and phonon properties of rutile TiO_2 at temperatures between 100 and 900 K using DFT calculations, lattice dynamics calculations, and the BTE. 0 K and finite-temperature FCs are extracted to examine and compare their impact on phonon frequencies, group velocities, lifetimes, and thermal conductivity. The 0 K FCs significantly underpredict the thermal conductivity along the *a* and *c* axes compared to available measurements, as shown in Figs. 2(a) and 2(b). Extracting FCs at each finite temperature leads to thermal conductivity predictions that are in better agreement with the measurements. We attribute the underpredicted thermal conductivities calculated by the 0 K FCs to an underprediction of phonon lifetimes [Fig. 5(b)], which in turn is a result of an overprediction of the three-phonon scattering phase space [Fig. 5(c)]. The finite-temperature anharmonic FCs are also essential to calculating the correct strength of each scattering process. In future work, it may be interesting to consider the effect of quadrupoles [74–77] on the phonon properties and thermal conductivity.

Our work demonstrates that extracting finite-temperature FCs is essential to predicting accurate phonon properties and thermal conductivity for rutile TiO_2. The strong temperature dependence of the FCs may also exist in other phases of TiO_2 (e.g., anatase, brookite) or other oxides. The frequency shifts and phonon scattering rates predicted from finite-temperature FCs are also critical for accurately predicting the dielectric functions of ceramics [42].

ACKNOWLEDGMENTS

This work was supported by the National Natural Science Foundation of China under Grants No. 51825604, No. 51721004, and No. 52130604. Olle Hellman provided the TDEP code and helpful guidance.

[1] J. Low, B. Cheng, and J. Yu, Appl. Surf. Sci. **392**, 658 (2017).
[2] Y. Yang, G. Liu, J. T. Irvine, and H.-M. Cheng, Adv. Mater. **28**, 5850 (2016).
[3] J. Low, B. Dai, T. Tong, C. Jiang, and J. Yu, Adv. Mater. **31**, 1802981 (2019).
[4] M. S. Ahmad, A. K. Pandey, and N. Abd Rahim, Renewable Sustainable Energy Rev. **77**, 89 (2017).
[5] Y.-Q. Wang, L. Gu, Y.-G. Guo, H. Li, X.-Q. He, S. Tsukimoto, Y. Ikuhara, and L.-J. Wan, J. Am. Chem. Soc. **134**, 7874 (2012).
[6] N. J. J. de Klerk, A. Vasileiadis, R. B. Smith, M. Z. Bazant, and M. Wagemaker, Phys. Rev. Mater. **1**, 025404 (2017).
[7] J. H. Braun, A. Baidins, and R. E. Marganski, Prog. Org. Coat. **20**, 105 (1992).
[8] R. Wang, K. Hashimoto, A. Fujishima, M. Chikuni, E. Kojima, A. Kitamura, M. Shimohigoshi, and T. Watanabe, Adv. Mater. **10**, 135 (1998).
[9] N. Nakamura, M. W. Terban, S. J. Billinge, and B. Reeja-Jayan, J. Mater. Chem. A **5**, 18434 (2017).
[10] H. Lee, R. C. Seshadri, S. J. Han, and S. Sampath, Appl. Energy **192**, 24 (2017).
[11] D. Isaak, J. Carnes, O. Anderson, H. Cynn, and E. Hake, Phys. Chem. Miner. **26**, 31 (1998).
[12] D. C. Cronemeyer, Phys. Rev. **87**, 876 (1952).
[13] R. Shirley, M. Kraft, and O. R. Inderwildi, Phys. Rev. B **81**, 075111 (2010).
[14] W. Kang and M. S. Hybertsen, Phys. Rev. B **82**, 085203 (2010).
[15] Y.-N. Wu, W. A. Saidi, P. Ohodnicki, B. Chorpening, and Y. Duan, J. Phys. Chem. C **122**, 22642 (2018).
[16] M. O. Atambo, D. Varsano, A. Ferretti, S. S. Ataei, M. J. Caldas, E. Molinari, and A. Selloni, Phys. Rev. Mater. **3**, 045401 (2019).
[17] K. A. McCarthy and S. S. Ballard, J. Opt. Soc. Am. **41**, 1062 (1951).
[18] F. Charvat and W. Kingery, J. Am. Ceram. Soc. **40**, 306 (1957).
[19] W. Thurber and A. Mante, Phys. Rev. **139**, A1655 (1965).
[20] P. Jiang, X. Qian, and R. Yang, Rev. Sci. Instrum. **88**, 074901 (2017).
[21] I. Yoshida, J. Phys. Soc. Jpn. **15**, 2211 (1960).
[22] J. H. Koenig, *Ceramic Research Station Progress Report 5* (Rutgers University, New Jersey, 1954).
[23] K. M. Ok, Y. Ohishi, H. Muta, K. Kurosaki, and S. Yamanaka, J. Am. Ceram. Soc. **101**, 334 (2018).
[24] Y. S. Touloukian, *Thermophysical Properties of Matter* (IFI/Plenum, New York, 1970).
[25] A. J. H. McGaughey, A. Jain, H.-Y. Kim, and B. Fu, J. Appl. Phys. **125**, 011101 (2019).
[26] A. Jain, Thermal transport in semiconductors and metals from first-principles, Ph.D. thesis, Carnegie Mellon University, Pittsburgh, PA, 2015.
[27] D. C. Wallace, *Thermodynamics of Crystals* (Cambridge University Press, Cambridge, UK, 1972).
[28] J. A. Reissland, *The Physics of Phonons* (Wiley, New York, 1973).
[29] A. Ward, First principles theory of the lattice thermal conductivity of semiconductors, Ph.D. thesis, Boston College, Boston, MA, 2009.
[30] B. Fu, K. D. Parrish, H.-Y. Kim, G. Tang, and A. J. H. McGaughey, Phys. Rev. B **101**, 045417 (2020).
[31] A. Taheri and C. V. Singh, Phys. Rev. Mater. **5**, 034009 (2021).
[32] H. L. Parks, H.-Y. Kim, V. Viswanathan, and A. J. H. McGaughey, Phys. Rev. Mater. **4**, 083805 (2020).
[33] B. Fu, G. Tang, and Y. Li, Phys. Chem. Chem. Phys. **19**, 28517 (2017).
[34] A. Ward, D. A. Broido, D. A. Stewart, and G. Deinzer, Phys. Rev. B **80**, 125203 (2009).
[35] L. Lindsay, D. A. Broido, and T. L. Reinecke, Phys. Rev. B **87**, 165201 (2013).
[36] L. Lindsay, W. Li, J. Carrete, N. Mingo, D. A. Broido, and T. L. Reinecke, Phys. Rev. B **89**, 155426 (2014).
[37] A. Jain and A. J. H. McGaughey, Sci. Rep. **5**, 8501 (2015).
[38] X. Tang and J. Dong, Proc. Natl. Acad. Sci. USA **107**, 4539 (2010).
[39] X. Wu, J. Lee, V. Varshney, J. L. Wohlwend, A. K. Roy, and T. Luo, Sci. Rep. **6**, 22504 (2016).
[40] M. D. Santia, N. Tandon, and J. Albrecht, Appl. Phys. Lett. **107**, 041907 (2015).
[41] L. Feng, T. Shiga, and J. Shiomi, Appl. Phys. Express **8**, 071501 (2015).
[42] Z. Tong, X. Yang, T. Feng, H. Bao, and X. Ruan, Phys. Rev. B **101**, 125416 (2020).
[43] L. Lindsay and D. S. Parker, Phys. Rev. B **92**, 144301 (2015).
[44] Y. Fu and D. J. Singh, Phys. Rev. Mater. **2**, 094408 (2018).
[45] G. Tompsett, G. Bowmaker, R. Cooney, J. Metson, K. Rodgers, and J. Seakins, J. Raman Spectrosc. **26**, 57 (1995).
[46] G. Fugallo, B. Rousseau, and M. Lazzeri, Phys. Rev. B **98**, 184307 (2018).
[47] B. Wehinger, A. Bosak, and P. T. Jochym, Phys. Rev. B **93**, 014303 (2016).
[48] T. Lan, C. W. Li, O. Hellman, D. S. Kim, J. A. Muñoz, H. Smith, D. L. Abernathy, and B. Fultz, Phys. Rev. B **92**, 054304 (2015).
[49] S.-M. Lee, D. G. Cahill, and T. H. Allen, Phys. Rev. B **52**, 253 (1995).
[50] D. Mitra, P. Howli, B. K. Das, N. S. Das, P. Chattopadhyay, and K. K. Chattopadhyay, J. Mol. Liq. **302**, 112499 (2020).
[51] H. Kangarlou and A. Abdollahi, Int. J. Thermophys. **37**, 110 (2016).
[52] E. Shojaee and M. Mohammadizadeh, J. Phys.: Condens. Matter **22**, 015401 (2009).
[53] B. Montanari and N. Harrison, Chem. Phys. Lett. **364**, 528 (2002).
[54] P. D. Mitev, K. Hermansson, B. Montanari, and K. Refson, Phys. Rev. B **81**, 134303 (2010).
[55] O. Hellman, I. A. Abrikosov, and S. I. Simak, Phys. Rev. B **84**, 180301(R) (2011).
[56] O. Hellman, P. Steneteg, I. A. Abrikosov, and S. I. Simak, Phys. Rev. B **87**, 104111 (2013).
[57] O. Hellman and I. A. Abrikosov, Phys. Rev. B **88**, 144301 (2013).
[58] P. Torres and R. Rurali, J. Phys. Chem. C **123**, 30851 (2019).
[59] N. Shulumba, O. Hellman, and A. J. Minnich, Phys. Rev. B **95**, 014302 (2017).
[60] N. Shulumba, O. Hellman, and A. J. Minnich, Phys. Rev. Lett. **119**, 185901 (2017).
[61] O. Hellman and D. A. Broido, Phys. Rev. B **90**, 134309 (2014).
[62] N. Shulumba, Z. Raza, O. Hellman, E. Janzén, I. A. Abrikosov, and M. Odén, Phys. Rev. B **94**, 104305 (2016).
[63] G. Kresse and J. Furthmüller, Phys. Rev. B **54**, 11169 (1996).
[64] G. Kresse and D. Joubert, Phys. Rev. B **59**, 1758 (1999).

[65] J. P. Perdew and A. Zunger, Phys. Rev. B **23**, 5048 (1981).
[66] K. Refson, B. Montanari, P. D. Mitev, K. Hermansson, and N. M. Harrison, Phys. Rev. B **88**, 136101 (2013).
[67] A. Togo, L. Chaput, and I. Tanaka, Phys. Rev. B **91**, 094306 (2015).
[68] See Supplemental Material at http://link.aps.org/supplemental/10.1103/PhysRevMaterials.6.015401 for information about the wave vector and supercell size convergence of the thermal conductivity, the thermal conductivity predictions from an in-house lattice dynamics code with inputs from QUANTUM ESPRESSO [78], phonon spectral functions at temperatures of 600 and 900 K, phonon group velocity from 600 K FCs and 900 K FCs, mean free path–dependent thermal conductivity accumulation functions, and phonon lifetimes and three-phonon scattering phase space from 600 K FCs.
[69] C. Yu, M. L. Scullin, M. Huijben, R. Ramesh, and A. Majumdar, Appl. Phys. Lett. **92**, 191911 (2008).
[70] To confirm the underprediction that results from the 0 K FCs, we used an in-house code [25,26] to perform the lattice dynamics calculations with an iterative solution of BTE based on DFPT and DFT calculations in QUANTUM ESPRESSO [78]. Even with different codes and pseudopotentials, we obtained similar results, as shown in Figs. S2(a) and S2(b) of the Supplemental Material [68].
[71] J. G. Traylor, H. Smith, R. Nicklow, and M. Wilkinson, Phys. Rev. B **3**, 3457 (1971).
[72] X. Gu, Z. Fan, H. Bao, and C. Y. Zhao, Phys. Rev. B **100**, 064306 (2019).
[73] L. Lindsay and D. Broido, J. Phys.: Condens. Matter **20**, 165209 (2008).
[74] G. Brunin, Henrique Pereira Coutada Miranda, M. Giantomassi, M. Royo, M. Stengel, M. J. Verstraete, X. Gonze, G.-M. Rignanese, and G. Hautier, Phys. Rev. Lett. **125**, 136601 (2020).
[75] G. Brunin, Henrique Pereira Coutada Miranda, M. Giantomassi, M. Royo, M. Stengel, M. J. Verstraete, X. Gonze, G.-M. Rignanese, and G. Hautier, Phys. Rev. B **102**, 094308 (2020).
[76] V. A. Jhalani, J.-J. Zhou, J. Park, C. E. Dreyer, and M. Bernardi, Phys. Rev. Lett. **125**, 136602 (2020).
[77] M. Royo, K. R. Hahn, and M. Stengel, Phys. Rev. Lett. **125**, 217602 (2020).
[78] P. Giannozzi, S. Baroni, N. Bonini, M. Calandra, R. Car *et al.*, J. Phys.: Condens. Matter **21**, 395502 (2009)